Generalized Modeling of Photoluminescence Transients

Max Großmann,* Sebastian Bohm, Stefan Heyder, Klaus Schwarzburg,
Peter Kleinschmidt, Erich Runge, and Thomas Hannappel

Time-resolved photoluminescence (TRPL) measurements and the extraction of meaningful parameters involve four key ingredients: a suitable sample such as a semiconductor double heterostructure, a state-of-the-art measurement setup, a kinetic model appropriate for the description of the sample behavior, and a general analysis method to extract the model parameters of interest from the measured TRPL transients. Until now, the last ingredient is limited to single curve fits, which are mostly based on simple models and least-squares fits. These are often insufficient for the parameter extraction in real-world applications. The goal of this article is to give the community a universal method for the analysis of TRPL measurements, which accounts for the Poisson distribution of photon counting events. The method can be used to fit multiple TRPL transients simultaneously using general kinematic models, but should also be used for single transient fits. To demonstrate this approach, multiple TRPL transients of a GaAs/AlGaAs heterostructure are fitted simultaneously using coupled rate equations. It is shown that the simultaneous fits of several TRPL traces supplemented by systematic error estimations allow for a more meaningful and more robust parameter determination. The statistical methods also quantify the quality of the description by the underlying physical model.

1. Introduction

Time-resolved photoluminescence (TRPL) is a superb method to characterize the dynamic properties of the minority charge carriers in semiconductor materials. Extracted parameters such as the minority charge carrier lifetimes can be used in quality control and in the design process of minority charge carrier devices such as solar cells,[1] solid-state lasers,[2] heterojunction bipolar transistors,[3] and light-emitting devices.[4] This contactless, noninvasive, nondestructive, and time-efficient analysis technique has been successfully used for several decades and is well documented.[5–9] The most important parameter for any minority charge carrier device is the bulk lifetime τ_B, which includes the radiative lifetime[10] τ_r and the nonradiative Shockley–Read–Hall (SRH) lifetime[11] τ_{nr}, which characterizes the nonradiative decay processes. In a realistic sample, in addition, surface and interface recombination processes contribute to the transient decay, characterized by the surface recombination velocity.[12] Gerber and Kleiman[13] showed that even in the absence of the latter processes, the extraction of the individual bulk parameters is generally not possible in a low-excitation regime, where the minority charge carrier density ρ is much smaller than the doping of the semiconductor $N_{D/A}$ because capture by and release from impurities dominate the transient dynamics. They solved this problem by modeling the charge carrier kinetics with different rate equations for different excitation levels and used these equations to fit their individually measured transients. Thereby, they disentangled different recombination channels and trapping mechanisms. Obviously, valid rate equations form the basis of any such approach. But even then, it is not clear without further assumptions which rate equation should be applied to which transient. One more fundamental approach is to describe the intensity-dependent dynamics of a sample using a coupled set of rate equations, which describe multiple TRPL transients all at once. Motivated by this challenge, we developed a more general method for the analysis of typical TRPL data, which is not limited to this example. The novelty of our work refers to the following properties of our method: the set of multiple transients with different initial excitation levels are fitted simultaneously by the full set of rate equations. Furthermore, we provide a mathematical framework based on maximum likelihood estimation (MLE), which takes the statistics of recombination processes into account and enables straightforward application of state of the art fitting algorithms to the data. While it is of course still necessary to obtain suitable

M. Großmann, S. Bohm, P. Kleinschmidt, E. Runge, T. Hannappel
Institut für Physik and Institut für Mikro- und Nanotechnologien
Technische Universität Ilmenau
98693 Ilmenau, Germany
E-mail: max.grossmann@tu-ilmenau.de

S. Heyder
Institut für Mathematik
Technische Universität Ilmenau
98693 Ilmenau, Germany

K. Schwarzburg
Institute for Solar Fuels
Helmholtz-Zentrum Berlin für Materialien und Energie GmbH
Hahn-Meitner-Platz 1, 14109 Berlin, Germany

measurement data and to choose a valid set of rate equations, our method then allows the reliable extraction of the different parameters governing the charge carrier recombination processes. The result of the fitting procedure also provides an indication of the validity of the chosen set of rate equations.

The article is organized as follows: we first motivate and formulate our approach in more general terms. Then, we formulate a specific physical model to describe the time evolution of photoluminescence (PL) in direct bandgap semiconductors. Afterward, we comment on the measurement technique used: time-correlated single photon counting (TCSPC). Using TCSPC implies a Poisson distribution for the number of photons counted, i.e., the measured intensity. In contrast to the case of the normal distribution, the variance of the Poisson distribution is equal to its mean. This is also called heteroscedasticity and poses problems for ordinary least squares (OLS) estimation.[14] We directly deal with the Poisson distribution by employing MLE, which maximizes the likelihood, i.e., the joint probability of the observations as a function of the model parameters.[15] The MLE estimates, in particular, have many desirable asymptotic properties: they are consistent, efficient, and normally distributed. Thus, one can quantify the uncertainty in the estimates by confidence intervals.[16] We need to emphasize that MLE is more suitable than OLS fitting because OLS disregards heteroscedasticity and does not allow for correct error estimation of the fitted parameters; therefore, MLE should also be used even for simple monoexponential fits to single TRPL transients.

The presented optimization procedure is tested using noisy synthetic data to check whether the high-dimensional global optimization problem can be solved with reasonable accuracy. Finally, we analyze TRPL measurements of a III–V semiconductor double heterostructure, which provides an application of our generalized modeling of time-resolved spectra to a practically relevant case.

2. Theory

The physical modeling of TRPL measurements is intrinsically difficult since a plethora of physical effects, whose relevance varies from sample to sample, influence the measured time-dependent intensity. Prior work on semiconductor TRPL addressed nonradiative recombination,[11,17] surface recombination,[12] trapping states,[8,13] self-absorption effects in III–V compound semiconductors,[18,19] and many other physical effects.[6,7,9] With a varying magnitude of initial density of excited charge carriers, the temporal dynamics varies between mono-, bi-, or nonexponential decay curves.[13] Generally speaking, previous and state-of-the-art TRPL modeling consists of explaining one transient at a time with a suitable approach accounting for one or more of the effects mentioned above.[12,13,20–22] This means that in extreme cases, a series of experimental (exp.) measurements, which contain multiple transients at different charge carrier injection levels $I^{exp.}(t)$, were explained one by one using predictions $I^{PL}(t, \rho^0)$ resulting from different parametric models $\mathscr{F}_i(t, \rho_i^0, \boldsymbol{p}_i)$

$$I_i^{exp.}(t) = I_i^{PL}(t, \rho_i^0) = \mathscr{F}_i(t, \rho_i^0, \boldsymbol{p}_i) \tag{1}$$

Here, the dependency on the initial injection level has been explicitly noted through the minority charge density ρ^0 at the time of injection. This means that one explains the i-th measurement $I_i^{exp.}$ with initial excitation ρ_i^0 through the excitation-specific parametric model $\mathscr{F}_i$, which depends on the parameters $\boldsymbol{p}_i$. Models like this have been mostly derived for a special range of injection levels $\{\rho_i^0\}$ in which typically one effect, such as trapping-based recombination or radiative recombination, dominates.[13]

To capture the underlying dynamical processes more thoroughly and to obtain more trustworthy physical parameters than those obtainable from Equation (1), we suggest to model a series of measurements with multiple transients at different injection levels all at once. However, realizing this suggestion requires a model that accounts simultaneously for all dynamical processes that are relevant at the different injection levels. We write

$$I_i^{exp.}(t) = I_i^{PL}(t, \rho_i^0) = \mathscr{F}(t, \rho_i^0, \boldsymbol{p}) \tag{2}$$

where $\mathscr{F}(t, \rho_i^0, \boldsymbol{p})$ now denotes a generalized TRPL model with the same parameter set $\boldsymbol{p}$ for all transients i. We emphasize that all experimental TRPL traces are subjected not only to external noise, but they also show at least at late times intrinsic variations resulting from the stochastic character of the signal at low photon counts. For PL, it is natural to assume that the signal is the sum of independent emissions of photons, which are counted, at least in TCSPC measurements, almost independently from each other. Mathematically, this translates into the assumption of a Poisson distribution for the photon counts. A model $\mathscr{F}$ aims at predicting "as good as possible" the expected transient $I_i^{PL}(t, \rho_i^0)$ by varying the parameters $\boldsymbol{p}$. From a mathematical point of view, we could have omitted ρ_i^0 on the right-hand side of Equation (2) and included it as one of the parameters $\boldsymbol{p}$. We retained the explicit ρ_i^0 dependence because on one hand, experimentalists would label their transients by the excitation level and, on the other hand, the theoretical modeling of TRPL is typically a theory for the position- and time-dependent minority charge density $\rho(\boldsymbol{r}, t)$. Most such models can be cast into the form of a reaction-diffusion system.

$$\frac{d\boldsymbol{q}}{dt} = \mathbf{D}\,\Delta\boldsymbol{q} + \mathbf{G}(\boldsymbol{q}) - \mathbf{R}(\boldsymbol{q}) \tag{3}$$

where the charge density vector function $\boldsymbol{q} = \boldsymbol{q}(\boldsymbol{r}, t)$ includes the charge density of the minority, majority, and trapping bands. The diagonal matrix $\mathbf{D}$ describes that charge is allowed to move inside each state through the semiconductor. The generation matrix $\mathbf{G}(\boldsymbol{q})$ and the recombination matrix $\mathbf{R}(\boldsymbol{q})$ include all possible and physically allowed transitions between the involved states such as trapping and multiple band-to-band transitions. Systems like Equation (3) have been suggested in many publications and are used all over physics, chemistry, and biology.[23–25]

A specific aspect of TRPL is that the charge carrier decay can be observed only indirectly via the time-dependent volume average of the radiative decay of the minority charge carriers.

$$I^{PL}(t, \rho^0) = \int_V \frac{1}{\tau_r(\rho(\boldsymbol{r}, t, \rho^0))} \rho(\boldsymbol{r}, t, \rho^0) \mathrm{d}V \tag{4}$$

where $\tau_{\mathrm{r}}(\rho(\boldsymbol{r}, t, \rho^0))$ denotes the respective minority charge carrier density-dependent time constant.[12]

2.1. Model Building

As a specific test case for our general approach, we now formulate a dynamical model based on the work of Gerber and Kleiman[13] for a type-I direct semiconductor double heterostructure with two trapping levels in the bandgap (see **Figure 1**). The main charge carrier recombination channels are the well-known and studied radiative[10] and nonradiative SRH[11] recombination, combined into the bulk lifetime $\tau_{\mathrm{B}}(\rho)$. We replace the minority charge carrier density ρ by the dimensionless fractional occupancy relative to the doping level $N_{\mathrm{D/A}}$, i.e., by $\eta = \rho/N_{\mathrm{D/A}}$. Following Gerber and Kleiman,[13] we parameterize the excitation dependence of the bulk lifetime via

$$\frac{1}{\tau_{\mathrm{B}}(\eta)} = \frac{1+\eta}{\phi\tau_{\mathrm{r}}^0} + \frac{1+\eta}{\tau_{\mathrm{nr}}^0(1+r\eta)} \qquad (5)$$

in terms of the low-excitation lifetime limits τ_{r}^0 and τ_{nr}^0 for the radiative decay and the nonradiative SRH decay, respectively. These parameters are the main performance indicator for minority charge carrier devices. While using Equation (5), we assume that $\Delta n = \Delta p$, where Δn is the excited electron density and Δp is the excited hole density.[13] The factor ϕ accounts for photon recycling.[18,26] The excitation-level dependence of the SRH recombination is characterized by a parameter $r = 1 + \sigma_{\min}/\sigma_{\max}$, which involves the ratio of the carrier trap capture cross sections for minority ($\sigma_{\min}$) and majority charge carriers ($\sigma_{\max}$).[13]

In the equilibrium state of continuous excitation, the trapping states inside the bandgap are filled and their influence on the charge carrier dynamics is negligible, i.e., the radiative and SRH recombination are the dominant effects in this case. However, during TRPL measurements, they dominate the transient dynamics in the low-excitation regime and, therefore, one needs to consider them to describe the physics of the transient decay accurately.[8,13] We added two trapping states to our model: trapping state 1 accounts for defects present inside the bandgap and is characterized by three time constants including one describing reemission into the conduction band. Trapping state 2 is motivated by the results of Redfield et al.[27] and can be thought of as a metastable deep trapping state because its decay time (τ_{2d}) is very large compared to all other time constants. It accounts for trapping processes with negligible reemission into the conduction band, which can be filled and saturated, in contrast to the SRH channel. Analogously to the introduction of η, the filling of the trapping states are described by the ratios $f_1 = n_1/N_1$ and $f_2 = n_2/N_2$ of filled levels to trap density.

All quantities are assumed to be spatially homogeneous, which holds true, e.g., in homogeneous samples if the excitation spot is much larger than the PL detection area. In particular,
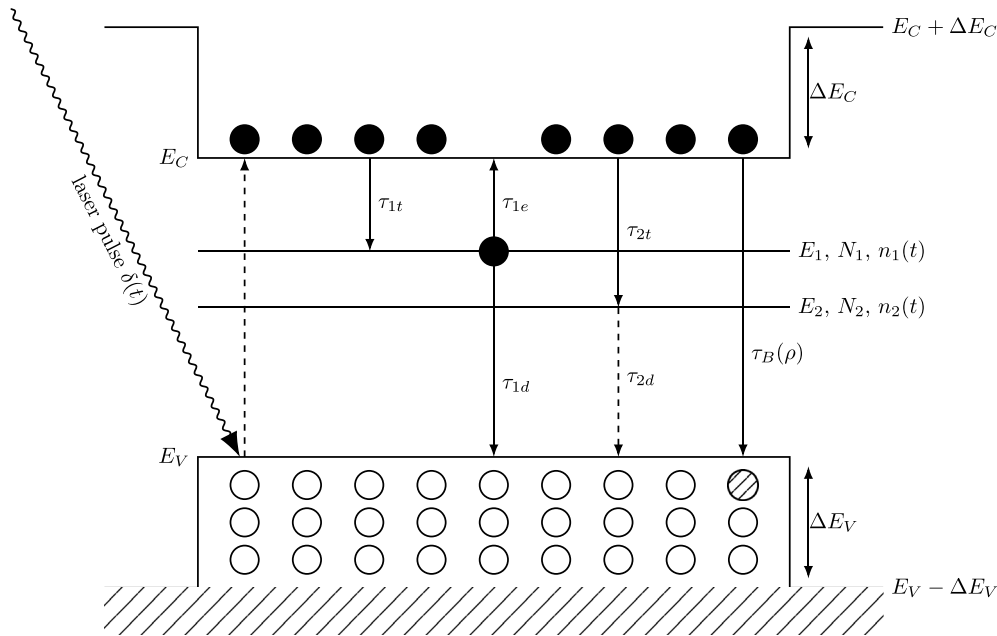

Figure 1. Schematic diagram of a type-I double heterostructure with a p-doped absorber region illustrating the dynamical processes included in our rate equation-based model. A short δ-like laser pulse excites electrons and creates an excess density ρ of minority charge carriers in the conduction band of the absorber. The minority charge carriers (electrons, filled circles) can recombine (dashed circles) with majority carriers (holes, empty circles) either radiatively and nonradiatively, predominantly via Shockley–Read–Hall (SRH) recombination. Both rates are combined into a density-dependent bulk time constant $\tau_{\mathrm{B}}(\rho)$. Alternatively, the minority charge carriers can get trapped into trapping states 1 and 2, at the energy levels E_1 and E_2, respectively. The position of trapping state 1 inside the bandgap is not further specified and captures charge carriers with a time-constant τ_{1t}. Carriers trapped in the trapping state 1 can be re-emitted to the conduction band with rate τ_{1e}^{-1} or decay back to the valence band at a rate τ_{1d}^{-1}. Trapping state 2 can be thought of as a metastable deep trapping state[13,27] with a trapping time-constant τ_{2t}, where the decay rate τ_{2d}^{-1} is assumed to be very small compared to all other transition (indicated by the dashed arrow). Other symbols denote level occupancies (see text) or the energetic alignment in the heterostructure.

inhomogeneity effects are ignored. At present, we also exclude effects such as surface recombination. This aspect is briefly discussed below. Thus, ignoring the *r*-dependence, using the abbreviations $\alpha = N_{D/A}/N_1$, $\beta = N_{D/A}/N_2$ and Equation (5), as well as the dynamical variables defined above and the process shown in Figure 1, one can derive the following rate equation system

$$
\begin{aligned}
\frac{d\eta(t)}{dt} &= \frac{1}{\alpha\tau_{1e}}f_1(t) - \frac{1+\eta(t)}{\phi\tau_r^0}\eta(t) - \frac{1+\eta}{\tau_{nr}^0(1+r\eta)}\eta(t) \\
&\quad - \frac{(1-f_1(t))}{\tau_{1t}}\eta(t) - \frac{(1-f_2(t))}{\tau_{2t}}\eta(t) \\
\frac{df_1(t)}{dt} &= \frac{(1-f_1(t))}{\tau_{1t}}\alpha\eta(t) - \left(\frac{1}{\tau_{1e}} + \frac{1}{\tau_{1d}}\right)f_1(t) \\
\frac{df_2(t)}{dt} &= \frac{(1-f_2(t))}{\tau_{2t}}\beta\eta(t)
\end{aligned}
\tag{6}
$$

We assume that the trapping states are empty before every excitation and, therefore, choose the following initial conditions: $\eta(0) = \eta^0$, $f_1(0) = 0$ and $f_2(0) = 0$, where η^0 is a model parameter, which can also be estimated experimentally as a comparison. Once $\eta(t)$ is known, the TRPL signal can be obtained from Equation (4) and (5) in the form

$$
\mathscr{F}(t, \boldsymbol{P}) = C\eta(t, \boldsymbol{P'})[1 + \eta(t, \boldsymbol{P'})]
\tag{7}
$$

Here, the total parameter vector $\boldsymbol{P}$ has the structure $\boldsymbol{P} = \{\boldsymbol{P'}, C\} = \{\boldsymbol{p}, \eta_1^0, \ldots, \eta_N^0, C\}$, where N denotes the number of measured TRPL transients. The parameter C contains experimental influences such as the detector efficiency and the total measurement time. For our particular model, $\boldsymbol{p}$ comprises 10 sample-dependent excitation-independent parameters.

Using data from one sample only, it is not straightforward to add surface recombination effects to our model because the surface recombination lifetime τ_S has an identical η dependence as the bulk SRH model (Equation (5)).[13] However, we expect that our method can be extended to disentangle the bulk- and surface-recombination lifetimes by measuring several otherwise identical samples with different absorber thicknesses. Again, simultaneous modeling of all transients of all samples is expected to yield more reliable parameter estimates.

2.2. Maximum Likelihood Estimation

Having developed a model for the measurements, one is now tasked with estimating the parameters $\boldsymbol{P}$ and quantifying the uncertainty in these estimates. As described in the introduction, one cannot use a least squares regression because the TRPL data are Poisson distributed. To this end, we employ the well-established framework of MLE.[28] Thus, we estimate $\boldsymbol{P}$ by minimizing the negative log-likelihood. To derive the negative log-likelihood, we index the measurements by a double index i,j where the first index identifies the i-th transient and the second identifies the j-th measurement in that transient at time t_j. For the i,j-th observation $I_{i,j}$ with expected value $\lambda_{i,j}(\boldsymbol{P}) = \mathscr{F}(t_j, \rho_i^0, \boldsymbol{p})$, the negative log-likelihood is $\lambda_{i,j}(\boldsymbol{P}) - I_{i,j}\log\lambda_{i,j}(\boldsymbol{P}) + \log(I_{i,j}!)$. Dropping the $\boldsymbol{P}$-independent last term, the total negative log-likelihood to be minimized is given by the sum

$$
l(\boldsymbol{P}) = \sum_{i=1}^{N}\sum_{j=1}^{M} \lambda_{i,j}(\boldsymbol{P}) - I_{i,j}\log\lambda_{i,j}(\boldsymbol{P})
\tag{8}
$$

because the fluctuations of the data points $I_{i,j}$ are statistically independent from each other. The minimizer $\widehat{\boldsymbol{P}}$ of Equation (8), i.e., the parameter set which minimizes Equation (8), is the maximum likelihood estimator of $\boldsymbol{P}$.

Standard asymptotic theory of maximum likelihood estimators[16] allows to obtain (asymptotic) confidence intervals for $\boldsymbol{P}$. Under some regularity conditions, the parameter uncertainty can be quantified through asymptotic pointwise confidence intervals based on a asymptotic normal distribution (details in the Supporting Information). For the i-th component of $\boldsymbol{P}$, we obtain such a confidence interval at confidence level $1-\alpha$ by $\widehat{P}_i \pm q_{1-\alpha/2}\sqrt{\mathbf{H}\left(\widehat{\boldsymbol{P}}\right)^{-1}_{i,i}}$. Here, $\mathbf{H}\left(\widehat{\boldsymbol{P}}\right)$ is the expected value, with respect to $I_{i,j}$, of the Hessian matrix of $l(\boldsymbol{P})$ at $\widehat{\boldsymbol{P}}$ and $q_{1-\alpha/2}$ is the $1-\frac{\alpha}{2}$ quantile of the standard normal distribution.

3. Experimental Methods

For a practical demonstration of the formalism developed above, we analyzed a set of TRPL transients of two unipolar $Al_xGa_{1-x}As|$p-GaAs$|Al_xGa_{1-x}As$ ($x = 0.509$) double heterostructures measured using TCSPC. We used TCSPC for the detection because it combines a large dynamical range and high temporal resolution. The samples were grown via metal–organic chemical vapor deposition (MOCVD) on a GaAs substrate. Both samples contained p-doped GaAs absorber layers with a thickness of 2000 nm and doping concentrations of $N_A = 5 \times 10^{16}$ cm^{-3} and $N_A = 10^{17}$ cm^{-3}, respectively. The $Al_xGa_{1-x}As$ barrier layers were p-doped with a bandgap of 1.92 eV and 100 nm thin.

The excitation source was the second harmonic of a 3 W pulsed ytterbium fiber laser (High Q femtoTRAIN IC-1040-3000 YB) at a wavelength of 520 nm with a pulse width of 250 fs. The light was then filtered by a 520 nm bandpass filter to block residuals of the lasers fundamental mode. To adjust the laser power, a motorized linear graded neutral density (ND) filter was used. The ND filter unit was calibrated before the experiment by measuring the photocurrent of a spectral calibrated silicon photodiode (PD) (**Figure 2**) as a function of the filter position. At a pulse repetition rate of 200 kHz, the maximum power at the sample position was 560 μW. The laser was passed through a custom-made 45° mirror with a center hole and then focused by 30 mm achromatic lens (L1) (Figure 2) onto the sample. In this configuration, the laser spot diameter was typically around 10 μm. To increase the illuminated area, a second lens (L2) (Figure 2) with a focal length of 200 mm was added to the beam path. This increased the spot diameter to a full width at half maximum of 205 μm. The beam diameter was measured by moving the edge of the wafer sample into the beam path via the sample translation stage while recording the photodiode current. The light emitted by the sample was collected and collimated by lens L1 and directed to the detection optics via the 45° mirror, where the light was filtered by a 800 nm longpass filter and ND filter to reduce the detector count rate to <10% of the laser repetition rate. The optical transmission of all ND
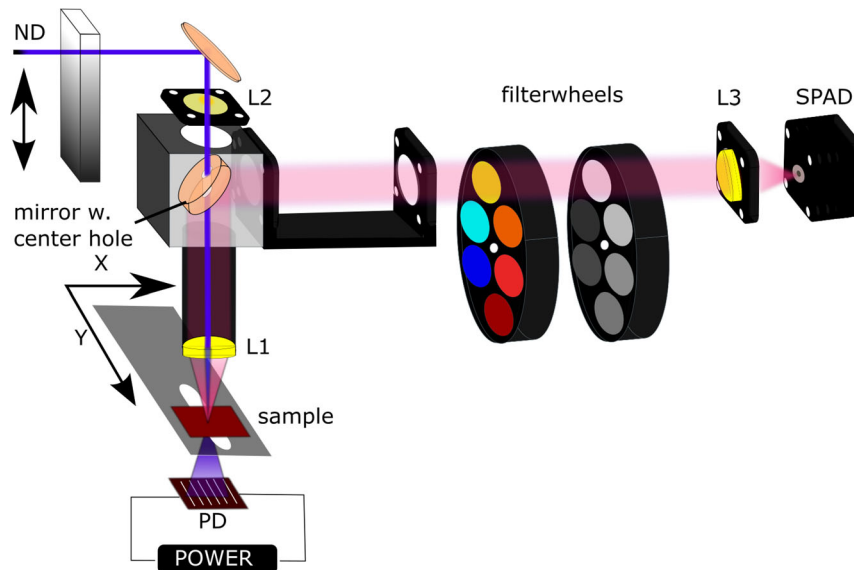
Figure 2. Schematic diagram illustrating the time-correlated single photon counting (TCSPC) measurement setup.

filters was measured directly before the experiment by using the sample's luminescent emission. Finally, the PL emission was focused with a 50 mm achromatic lens onto the photon counting avalanche photodiode (Micro Photon Devices—Model MPD, 50 μm detector diameter, dark count rate < 50 cts s^{-1}).

As a trigger source for the photon counting unit (PicoQuant PicoHarp PH 300[29]), a small fraction of the laser beam was focused to a fast photodiode and the electrical output was amplified by 20 dB.

While the PicoHarp counter had a built-in 16-bit histogram mode to directly record decay curves, we had used here the more flexible time-tagged time-resolved (TTTR) T2 mode of the unit.[29] Trigger and photon events were recorded as individual 32-bit time tags events. Each 32-bit value encoded a time stamp as well as channel and marker information. The measuring mode allowed to preserve the full event history for an arbitrary recording time with a temporal resolution of ≈40 ps between trigger and photon events. As a result, the histogram dynamic bit depth was only limited by the numerical tools used (here 64 bit) and the full-time resolution was preserved. Data recorded in T2 mode also allowed to exclude secondary photon events from the histogram at the analysis stage. All secondary photon events were excluded to minimize afterpulsing artifacts of the single-photon avalanche diode (SPAD).

For each sample, we measured five transients with an exponentially increasing laser power P. Starting at the lowest possible excitation power of our setup of around $P_1 = 70$ nW, we incremented P approximately by power of 10 up to the maximum laser power of $P_5 = 0.6$ mW. The transients were measured using a time span of 2000 ns with a total measurement time of 1000 s per transient. After each measurement, we binned the transient data to a temporal resolution of 0.25 ns. The experimentally measured transients all exhibited a strong excitation-dependent shape, which could, in some cases, originate from charge carrier separation at heterojunctions.[30–32] In our layer structure, we could exclude the influence of charge carrier separation due to internal electric fields on the TRPL measurements because of the

very high electron mobility of GaAs in the absorption layers of the unipolar double heterostructures ($\mu_n^p > 1000$ cm^2 V^{-1} s^{-1}).[33,34] The axial diffusion time of excited electrons, which represented an upper limit to the decay time in the presence of built-in fields, was, therefore, <1 ns and would result in a much shorter decay time than observed in the experiment.[35] In this case, the PL decay would be dominated by the drift time of charge carriers created within the depletion layer with a decay time in order of a few picoseconds. Since the experimental time resolution is ≈40 ps, this would be clearly observable experimentally.

For the following optimization procedure, we used the transients starting from their maximum until the transient with the highest initial excitation reached the noise floor. The uncut transients and cut transients can be found in the Supporting Information. The background counts b_i were estimated by averaging the noise floor at the end of each transient i. The model described in Equation (7) can be improved by the inclusion of experimental parameters

$$\mathscr{F}_i(t, \boldsymbol{P}) = \tilde{C} \frac{I_{max}^{exp.}}{ND_i} \eta(t, \boldsymbol{P})[1 + \eta(t, \boldsymbol{P})] + b_i \tag{9}$$

where $\mathscr{F}_i(t, \boldsymbol{P})$ represented the i-th transient of the shared kinetic model $\mathscr{F}(t, \boldsymbol{P})$, ND_i is the optical density of the neutral density filters used in the experiment during the measurement of transient i, and b_i is the averaged background noise described above. Further information about these parameters can be found in the Supporting Information. We additionally rescaled the experimental constant C by the maximum number of counts $I_{max}^{exp.}$ to $\tilde{C}$, improving the convergence and stability of the optimization procedure as described below.

4. Computational Methods

We developed our open-source optimization procedure[36] in *Julia*. The rate-equation system Equation (6) was solved using

**ADVANCED
SCIENCE NEWS**

www.advancedsciencenews.com

physica pssb
status
solidi

www.pss-b.com

the *DifferentialEquations.jl*[37] package. The optimization processes involve two steps: a global derivative-free optimizer[38,39] followed by a local derivative-based optimizer.[40] Because our optimization objective involves a noisy loss function $l(\boldsymbol{P})$, we repeated the global optimization multiple times using random initial conditions. To find the best optimization result, we used the following heuristic: each global optimization was followed-up by a local derivative-based optimizer. Afterward, the best result of all runs was then optimized again using a reparameterized loss function (Equation (8)) with the same local derivative-based optimizer. We used the following reparameterization

$$\tilde{\tilde{\boldsymbol{P}}} = \mathbf{S} \cdot \hat{\boldsymbol{P}} \quad \text{with} \quad \mathbf{S} = \text{diag}\left(10^{-\left\lfloor \log_{10}\left(\hat{P}_i\right)\right\rfloor}\right) \tag{10}$$

where $\hat{\boldsymbol{P}}$ corresponds to the best result of all prior global optimizations and $\lfloor \cdot \rfloor$ represents the floor function. This transformation improves the convergence properties of the local derivative-based optimization by drastically decreasing the condition number of the Hessian matrix of $l(\boldsymbol{P})$. It is also useful when calculating the confidence intervals through the unscaled inverse expected Hessian matrix:

$$\mathbf{H}\left(\hat{\boldsymbol{P}}\right)^{-1} = \mathbf{S}^{-1}\mathbf{H}\left(\tilde{\tilde{\boldsymbol{P}}}\right)^{-1}\mathbf{S}^{-1} \tag{11}$$

Further information on the exact algorithms, programs, and packages used in our method can be found in the Supporting Information.

5. Results and Discussion

5.1. Synthetic Data Analysis

We tested our procedure on five synthetic data sets, using parameters inspired by the results of Gerber and Kleiman with initial conditions achievable with our experimental setup and realistic values for ND_i and b_i [see Equation (9) and the Supporting Information]. Three of the data sets contain five transients (data sets 1, 2, and 3), and the others contain six transients. We set the factor $I_{max}^{exp.} = 10^6$ from Equation (9) for all synthetic data sets and added Poisson noise to each synthetic data set to simulate real measurement data. We performed 25 optimization runs per data set with 2.5×10^6 iterations during each run. We used very generous bounds during all global optimizations and none in the local optimizations (see Supporting Information), practically making the optimization unconstrained. In the following, we will only show the results of the synthetic data set 1. The results for
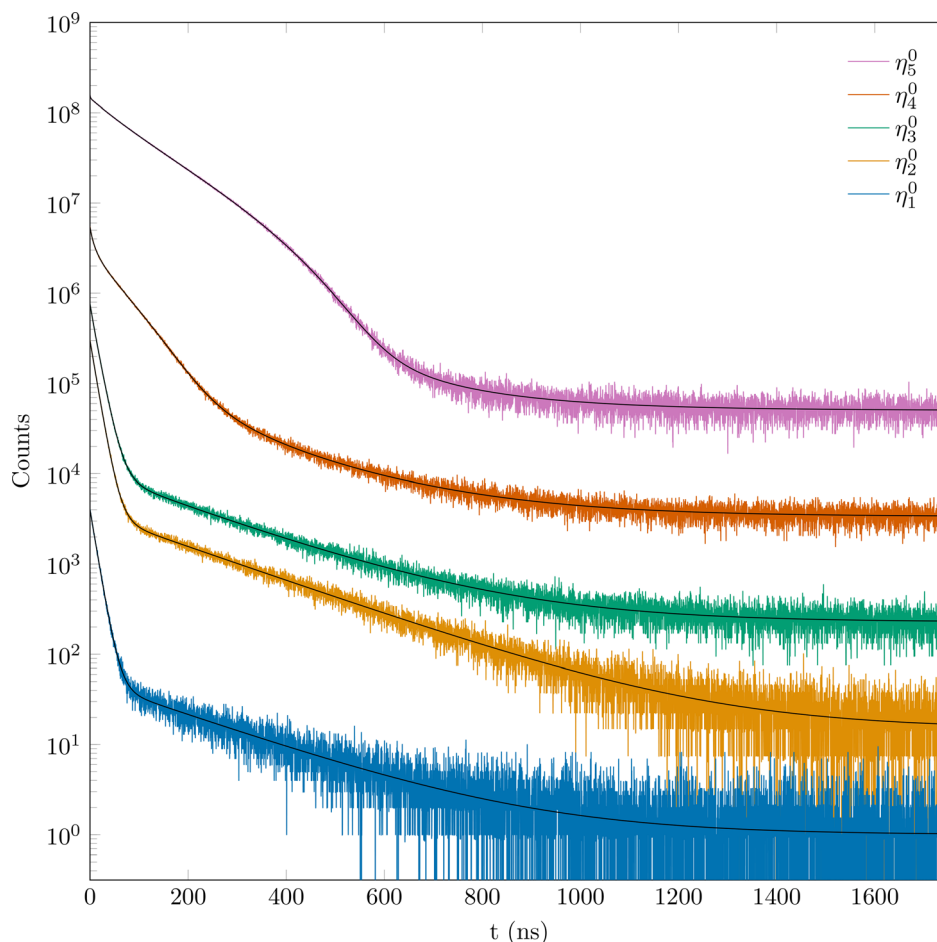

Figure 3. Simulated synthetic data set 1 with Poisson noise (colored lines) and fits (solid black lines) created with parameters from Table 1 and 2. All displayed transients are scaled for visual clarity, i.e., shifted against each other on the log scale.

Table 1. Initial conditions η^0_{true} and η^0_{fit} used to create the noisy synthetic data set 1 and fits in Figure 3, respectively.

Transient	1	2	3	4	5
η^0_{true}	4.00×10^{-5}	4.00×10^{-4}	4.00×10^{-3}	4.00×10^{-2}	4.00×10^{-1}
η^0_{fit}	4.02×10^{-5}	4.00×10^{-4}	4.00×10^{-3}	4.00×10^{-2}	4.00×10^{-1}
CIHW(95%)	4.25×10^{-6}	4.23×10^{-5}	4.21×10^{-4}	4.11×10^{-3}	3.37×10^{-2}
δ [%]	0.40	0.09	0.01	0.11	0.07

Table 3. Average relative parameter errors for each synthetic data set.

Data set	1	2	3	4	5
$\overline{\delta}$ [%]	1.9143	3.8032	3.4968	0.8204	0.7549

the other four synthetic data sets can be found in the Supporting Information.

The results for the synthetic data set 1 are shown in **Figure 3**. The input and fit initial conditions and parameters can be found in **Table 1** and **2**. They include the obtained fit parameters and initial conditions, and their 95% confidence interval half widths (CIHW) and relative errors with respect to the true parameters δ. The uncertainty in the estimates is captured in the 95% confidence intervals, which seem to be properly calibrated; they contain the true parameters in almost all cases. All synthetic tests converged close to the true parameters, indicating that the optimization problem can be solved with great accuracy. The average relative parameter error $\overline{\delta}$ of the fitted parameter with respect to the true parameters stayed below 4% for all data sets (see **Table 3**).

The observed small deviations from the true parameters are to be expected due to the stochastic nature of the simulated data sets. We explored the quality of the synthetic data fits further by analyzing the deviance residuals[41] in Section 5.3.

5.2. Experimental Data Analysis

The measured transients were analyzed in the same way as the synthetic data sets with the model previously described. We roughly estimated the expected η^0 using experimental parameters and the sample composition in conjunction with optical constants from Ref. [42] and transfer matrix theory from Ref. [43] (calculation details can be found in the Supporting Information) to compare them to the fit parameters. We estimate that the approximation of the experimental η^0 was subjected to a deviation of order 10%.

Here, we present the analysis of a single TRPL measurement and provide the results of a further sample in the Supporting Information (Figure S11, Table S16, S17, Supporting Information). Therefore, we will only discuss the results of sample 1, but all statements hold true for sample 2 as well.

The resulting fit of sample 1 is shown in **Figure 4**. The fit explains the experimental data exceptionally well, showing that the proposed model is well suited to analyze III–V semiconductor heterostructures. We explore the quality of this fit further by analyzing the deviance residuals[41] in the following Section 5.3.

The approximated $\eta^0_{exp.}$ from **Table 4** agrees well with the fitted initial conditions η^0_{fit} from Table 4, considering the uncertainty in the experimental η^0 approximation. The radiative lifetime τ^0_r of sample 1 is around 1.75 times larger than the value extracted from the measurement data of sample 2 (see Table S17, Supporting Information), which is in good agreement with around two times higher doping density of sample 2. The parameter τ_{1e} and the associated CIHW from **Table 5** indicate that the assumed transition from the trapping state 1 to the conduction band is either extremely unlikely or not present. Previous analysis methods of TRPL transients would fit a transient at low excitation levels with a monoexponential model $\mathcal{F}_{mono}(A, \tau^{eff}_{mono}, b, t) = A \cdot \exp(-t/\tau^{eff}_{mono}) + b$ in terms of an effective charge carrier lifetime τ^{eff}_{mono} and an unspecified constant A.[44,45] Using our introduced framework, it is now possible to decouple τ^{eff}_{mono} into basic recombination and trapping lifetimes, meaning that

$$\frac{1}{\tau^{eff}_{sum}} = \frac{1}{\phi\tau^0_r} + \frac{1}{\tau^0_{nr}} + \frac{1}{\tau_{1t}} + \frac{1}{\tau_{1e}} + \frac{1}{\tau_{1d}} + \frac{1}{\tau_{2t}}. \quad (12)$$

To illustrate and test this feature, we fitted the transients of both sample measured at the lowest laser pulse power by minimizing Equation (8), substituting $\lambda_{i,j}(\mathbf{P})$ with $\mathcal{F}_{mono}(A, \tau^{eff}_{mono}, b, t)$. The resulting fits can be found in the Supporting Information. For sample 1, we calculated an effective lifetime through Equation (12) of $\tau^{eff}_{sum} = 6.30 \pm 0.01$ ns and the monoexponential fit yielded $\tau^{eff}_{mono} = 6.06 \pm 0.03$ ns. These results show that the effective lifetime can be a misleading performance indicator for minority charge carrier semiconductor devices because the SRH lifetime τ^0_{nr} (see Table 5) is large compared to both τ^{eff}, which are dominated by the trapping lifetime τ_{1t}. The trapping transitions, however, barely influence the device performance under continuous illumination, making the SRH lifetime the major performance indicator, which is not well represented by the effective lifetime. The r value of the SRH

Table 2. Synthetic input parameters p_{true} and fit parameters p_{fit} used to create the noisy synthetic data set 1 (colored lines) and fits (black lines) displayed in Figure 3. All time constants τ are given in ns, while the other parameters are dimensionless.

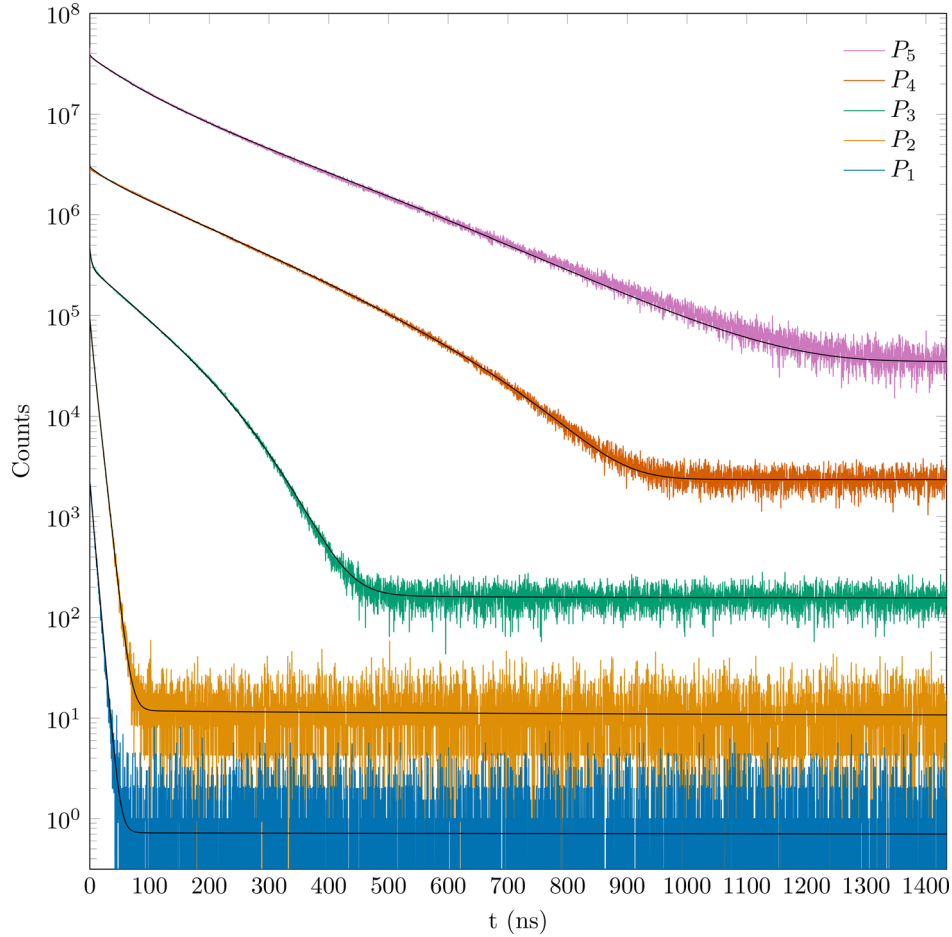|	$\phi\tau^0_r$	τ^0_{nr}	r	τ_{1t}	τ_{1e}	τ_{1d}	α	τ_{2t}	β	$\tilde{C}$
p_{true}	175.00	350.00	20.00	20.00	800.00	250.00	70.00	60.00	110.00	1.00×10^3
p_{fit}	175.00	355.00	19.39	19.90	808.00	250.00	69.30	61.10	111.00	9.99×10^2
CIHW	8.58	42.20	4.22	0.26	11.90	1.20	6.87	2.03	12.90	1.06×10^2
δ [%]	0.16	1.42	3.05	0.70	0.99	0.14	1.04	1.89	1.13	0.12

Figure 4. Processed measurement data from sample 1 (colored lines) and fits (black lines) created with parameters from Table 4 and 5. Transients are ordered by the magnitude of their initial excitation with a laser pulse of power P from bottom to top ($P \propto \eta^0$). All displayed transients are scaled for visual clarity, i.e., shifted against each other on the log scale.

Table 4. Laser pulse power P, experimental approximation of the initial conditions $\eta^0_{\mathrm{exp.}}$, fitted initial conditions η_{fit}, and 95% confidence interval half-widths CIHW of η_{fit} for sample 1.

Transient	1	2	3	4	5
$P[\mu W]$	6.94×10^{-2}	6.95×10^{-1}	6.96	6.95×10^1	6.21×10^2
$\eta^0_{\mathrm{exp.}}$	8.91×10^{-5}	8.92×10^{-4}	8.93×10^{-3}	8.92×10^{-2}	7.97×10^{-1}
η^0_{fit}	9.81×10^{-5}	9.77×10^{-4}	1.09×10^{-2}	9.51×10^{-2}	7.46×10^{-1}
CIHW	6.14×10^{-6}	6.04×10^{-5}	6.69×10^{-4}	5.45×10^{-3}	3.30×10^{-2}

recombination term (see Equation (5)) lies within the range given by Gerber and Kleiman and most likely hints at the presence of EL2 defects.[46] The estimated effective density of states of the metastable deep trapping levels is higher than the typical value found in the literature for EL2 defects in GaAs/AlGaAs heterostructures[47]: $N_2 \geq 5 \times 10^{13}$ cm^{-3}. Therefore, it is reasonable to assume that multiple deep-level defects contribute to N_2, weighted by their capture cross sections. Assuming quasi-equilibrium boundary conditions, we can use $\rho_1 = N_{\mathrm{C/V}} \exp(-|E_1 - E_{\mathrm{C/V}}|/k_{\mathrm{B}}T)$ and $(\tau_{1t}/\tau_{1e}) = (\rho_1/N_1)$ to

Table 5. Model parameters p_{fit} and 95% CIHW for sample 1. All time constants τ are given in ns, N_1, and N_2 in cm^{-3}. The other parameters are dimensionless.

	$\phi\tau_r^0$	τ_{nr}^0	r	τ_{1t}	τ_{1e}	τ_{1d}	N_1	τ_{2t}	N_2	$\bar{C}$
p_{fit}	253.00	385.00	30.77	6.85	437000.00	1190.00	1.91×10^{14}	189.00	8.78×10^{14}	1.10×10^4
CIHW	7.03	14.10	4.30	0.02	72700.00	10.00	1.17×10^{13}	0.68	4.63×10^{13}	6.82×10^2

calculate the band offset $|E_1 - E_{C/V}|$ between the trapping level 1 and the majority band through the following Equation (13)

$$|E_1 - E_{C/V}| = -k_B T \ln\left(\frac{\tau_{1t} N_1}{\tau_{1e} N_{C/V}}\right) \quad (13)$$

With the effective density of state $N_{C/V}$ from Blakemore[48] and $k_B T = 25.7$ meV, we obtained a very large value for $E_1 - E_V = (0.5623 \pm 0.003)$ eV. This indicates that the assumed trapping level 1 is actually not shallow, which would also explain the extremely large τ_{1e}. One can now make an educated guess using the data from Sze and Irvin[33] that our sample may have had some exposure to iron during its preparation. It could also be possible that the trapping state 1 stems from donor levels.[33] These guesses still need to be validated through additional measurements.

As a final point, one needs to discuss the interpretation of SRH lifetime in our model in presence of the two additional trapping states; Gerber and Kleiman showed that two different trapping states are needed to explain the data at low excitations.[13] For this reason, we have also built our model with two trapping states and achieve good results as presented. This can be motivated by the following observations. The SRH model does not include the time-dependent trap dynamics. The SRH lifetime[11] at low excitations simplifies to a constant lifetime. Furthermore, the SRH model just captures the excitation dependence of one trapping state deep inside the bandgap. Trapping state 1 allows for detrapping, which is not included in the SRH model. The inclusion of trapping state 2 is debatable, but introduced trapping states are included to aid the constant SRH lifetime at low excitations through their explicit inclusion into the rate equations, thereby gaining a time-dependent trap dynamic. In this sense, the trapping state 2 can be thought of as an extension to the SRH model at low excitations. From the point of view of a theoretical physicist, the main difference between trapping state 2 and the SRH recombination is that trapping state 2 can be saturated, while the SRH does not saturate in the presented parameterization. The authors believe that the SRH lifetime can still be interpreted in the same way as before when comparing different materials, as it can be regarded as an additional third trapping state, but this aspect should be further investigated in future publications.
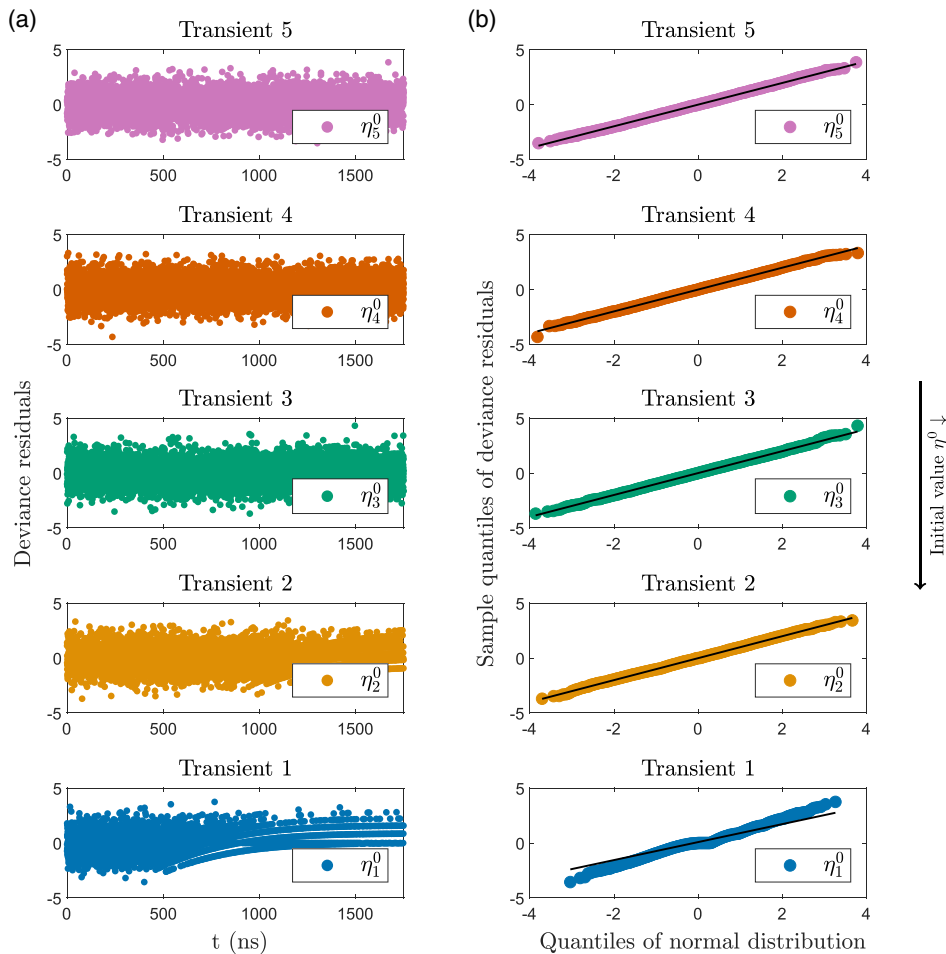

Figure 5. Residual analysis for synthetic data set 1: a) deviance residuals $D_{i,j}$ for each time t_j and each transient i. Except for discretization effects at low intensities (large times t), we see white noise in these plots. b) Q–Q plot for the quantiles of our residuals compared with those from the standard normal distribution. As expected, one obtains more or less straight lines. Deviations at the lower and upper ends are attributed to discretization effects for low intensities.

5.3. Residual Analysis

In addition to modeling, an easily accessible method for the validation of the used model $\mathscr{F}(t, \widehat{P})$ is desirable. One easy to implement possibility to do such a validation is to perform a residual analysis. Therefore, the deviance residuals[41] $D(t_j, \rho_i^0)$ for the Poisson distribution are computed, meaning that every count $I_{i,j}$ of the transient i at time j is compared to the prediction of that count in the model $\lambda_{i,j}(\widehat{P})$. The residuals are calculated via

$$D_{i,j} = \text{sgn}\left(I_{i,j} - \lambda_{i,j}(\widehat{P})\right) \sqrt{2\left[I_{i,j}\log\left(\frac{I_{i,j}}{\lambda_{i,j}(\widehat{P})}\right) - \left(I_{i,j} - \lambda_{i,j}(\widehat{P})\right)\right]}$$

(14)

taking the nonconstant variance of the Poisson distribution through the log-likelihood into account. If modeled correctly, one would expect that the deviance residuals follow an approximate standard normal distribution at least in the case of high intensities. For low intensities (large times t), this will not be the case due to the discrete nature of the Poisson distribution.

We conducted a standard residual analysis for the five synthetic and two experimental data sets introduced previously. Therefore, we checked whether the distribution of the deviance residuals changes by plotting them as a function of time. Except for discretization effects in the regime of low intensities, one would expect to see white noise in these plots. In addition, we investigated how closely the distribution residuals resemble a normal distribution using quantile–quantile (Q–Q) plots, comparing the sample quantiles of the residuals with those from the standard normal distribution. In these figures, one would expect a linear relationship, indicating that the residuals follow a normal distribution. It becomes clear that this is fulfilled reasonably well (see **Figure 5** and **6**). However, discretization effects become visible as discrepancies from the linear curve at the lower and upper ends.

The residual plots for the synthetic fits show the expected behavior (see Figure 5a), i.e., white noise except for discretization
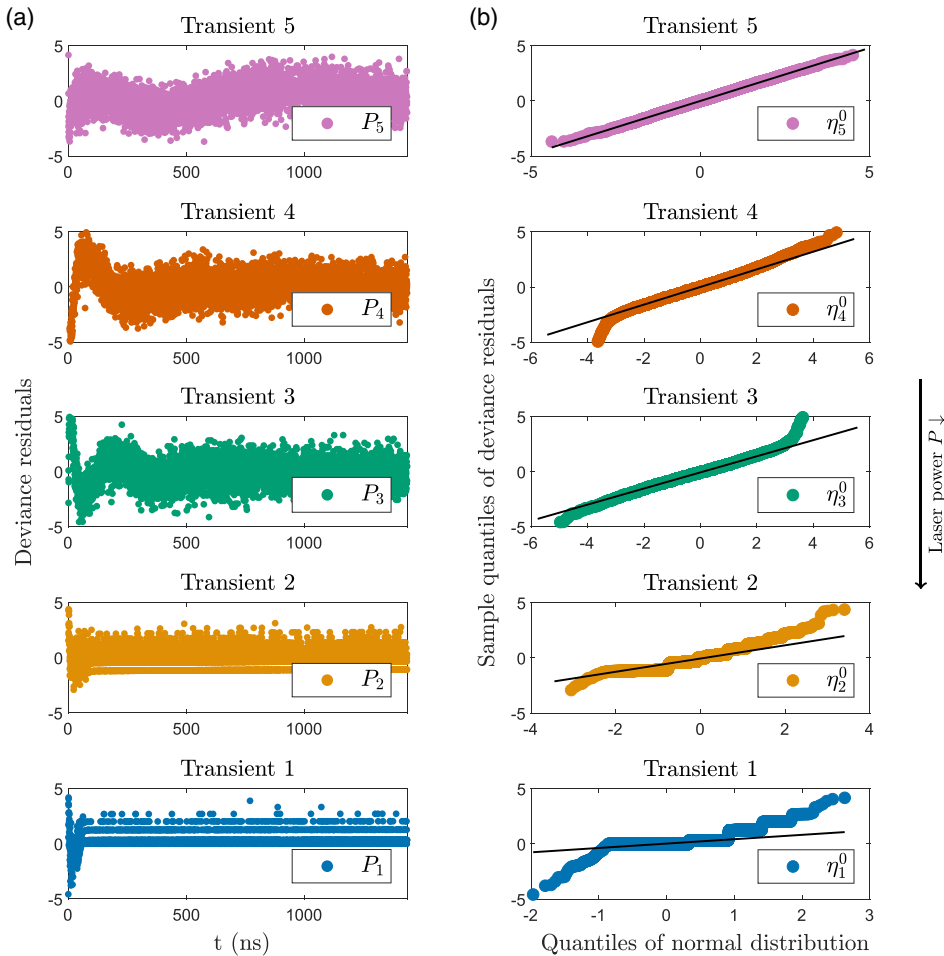

Figure 6. Residual analysis for sample 1: a) deviance residuals $D_{i,j}$ for each time t_j and each transient i. Due to discretization effects at low intensities (large times t), we see a deviations from the expected white noise in these plots. In addition, we observe for low t, i.e., high intensities, a slight misfit in the models. b) Q–Q plot for the quantiles of our residuals compared with those from the standard normal distribution. We expect and mostly see straight lines. Deviations at the lower and upper ends are attributed to discretization effects for low intensities and a slight misfit in the models for low t, i.e., high intensities.

effects for low intensities. The Q–Q plots (see Figure 5b) display no discernable change in the distribution of residuals. This result is, on one hand, expected due to the good reconstruction of parameters (see Table 3), but, on the other hand, important to verify because of the nonlinear dependence of the intensities on the parameters P, as well as the high dimensionality and nonconvexity of the optimization problem involved.

In the residual analysis of the experimental fits (see Figure 6a), we see, similar to the residual analysis for the synthetic data sets, discretization effects in transients measured at low intensities. In addition, we observe for high intensities, a slight misfit in the models. This is visible, for example, in the transients 3 and 4 of sample 1, both in the residuals themselves and associated Q–Q plots (see Figure 6a,b). We attribute this effect either to the preprocessing of the measured data, in particular to the truncation of the transients at their maximum, or to a fast relaxation process that occurs only at higher intensities which is not perfectly captured by the model. We note that except for these deviations, the residuals and Q–Q plots closely resemble those of the synthetic data.

In total, we conclude that the model and method of estimation by MLE produce results with high goodness of fit both for the synthetic data and for real measurement data. In future work, one may investigate the deviations at higher intensities even closer, further improving the fit for real measurements. The results of the residual analysis for all individual data sets can be found in the Supporting Information.

6. Conclusion

A general framework to analyze TRPL measurements was developed. This framework differs from common analysis methods in such a way that a complete excitation-dependent set of TRPL transients is fitted with a full set of rate equations simultaneously using MLE, which takes photon statistics into account and provides an uncertainty estimate.

As a proof of concept, the method was tested successfully on five noisy synthetic data sets and two measurements of prototypical GaAs/AlGaAs double heterostructures using a rate-equation model inspired by the work of Gerber and Kleiman.[13] Our framework allowed excellent fitting of the data and correctly reconstructed the initial condition, which were validated by an estimate using experimental parameters. Our approach allows a quantification of the uncertainty in the estimated parameters by confidence intervals, making a quantitative analysis of the accuracy of the inferred parameters possible. In addition, we show that it is possible to assess the quality of the applied physical model through a residual analysis of the fits, helping the community find appropriate models more easily.

Furthermore, we supply the community with scripts, programs, and data used in this article[36] to give everyone the opportunity to apply our method to their own measurements using their own kinetic models. Therefore, we are convinced that our general framework provides a powerful tool to analyze TRPL transients for perovskite solar cells and organic semiconductor using suitable models, aiding in the assessment of the quality and properties of a solar cell absorber materials.

In the future, one could extend this model using the introduced method to include surface and interface recombination by applying it to measurement data from a set of samples with varying absorber thickness, increasing the physical understanding of the recombination dynamics of minority charge carriers in semiconductors.

In summary, we provided a new way to analyze TRPL measurements using a simultaneous explanation of multiple transients via rate equation-based physical models by applying modern statistical and numerical methods, thereby improving future analysis of TRPL measurements drastically.

Supporting Information

Supporting Information is available from the Wiley Online Library or from the author.

Conflict of Interest

The authors declare no conflict of interest.

Data Availability Statement

The data that support the findings of this study are openly available in "Generalized modelling of photoluminescence transients" at http://doi.org/10.5281/zenodo.7178576.

[1] W. Shockley, H. J. Queisser, *J. Appl. Phys.* **1961**, *32*, 510.

[2] H. Y. Ryu, K. H. Ha, J. H. Chae, K. S. Kim, J. K. Son, O. H. Nam, Y. J. Park, J. I. Shim, *Appl. Phys. Lett.* **2006**, *89*, 171106.

[3] B. Lye, P. Houston, C. Button, J. David, *Solid-State Electron.* **1998**, *42*, 115.

[4] J. Müller, H. Reichl, H. Bernt, *Solid-State Electron.* **1979**, *22*, 257.

[5] R. K. Ahrenkiel, in *Minority Carriers In III-V Semiconductors: Physics and Applications* (Ed. R. K. Ahrenkiel, M. S. Lundstrom), Semiconductors and Semimetals, Vol. 39, Elsevier, Amsterdam **1993**, pp. 39–150.

[6] M. Maiberg, R. Scheer, *J. Appl. Phys.* **2014**, *116*, 123711.

[7] M. Maiberg, R. Scheer, *J. Appl. Phys.* **2014**, *116*, 123710.

[8] M. Maiberg, T. Hölscher, S. Zahedi-Azad, R. Scheer, *J. Appl. Phys.* **2015**, *118*, 105701.

[9] M. Maiberg, F. Bertram, M. Müller, R. Scheer, *J. Appl. Phys.* **2017**, *121*, 085703.

[10] E. Yablonovitch, T. J. Gmitter, R. Bhat, *Phys. Rev. Lett.* **1988**, *61*, 2546.

[11] W. Shockley, W. T. Read, *Phys. Rev.* **1952**, *87*, 835.

[12] R. K. Ahrenkiel, *Solid-State Electron.* **1992**, *35*, 239.

[13] M. W. Gerber, R. N. Kleiman, *J. Appl. Phys.* **2017**, *122*, 095705.

[14] J. Fox, *Applied Regression Analysis and Generalized Linear Models*, 3rd ed., SAGE, Los Angeles **2016**.

[15] R. Berger, G. Casella, *Statistical Inference*, 2nd ed., Duxbury Press, Florence, AL **2001**.

[16] A. W. Van der Vaart, *Asymptotic Statistics*, Cambridge University Press, Cambridge **2000**.

[17] D. Debuf, Y. Shrivastava, A. Dunn, *Phys. Rev. B* **2002**, *65*, 245211.

[18] P. Asbeck, *J. Appl. Phys.* **1977**, *48*, 820.

[19] R. K. Ahrenkiel, D. J. Dunlavy, B. Keyes, S. M. Vernon, T. M. Dixon, S. P. Tobin, K. L. Miller, R. E. Hayes, *Appl. Phys. Lett.* **1989**, *55*, 1088.

[20] Y. Xing, L. Wang, D. Yang, Z. Wang, Z. Hao, C. Sun, B. Xiong, Y. Luo, Y. Han, J. Wang, H. Li, *Sci. Rep.* **2017**, *7*, 45082.

[21] A. A. B. Baloch, F. H. Alharbi, G. Grancini, M. I. Hossain, M. K. Nazeeruddin, N. Tabet, *J. Phys. Chem. C* **2018**, *122*, 26805.

[22] L. Krückemeier, B. Krogmeier, Z. Liu, U. Rau, T. Kirchartz, *Adv. Energy Mater.* **2021**, *11*, 2003489.

[23] A. M. Turing, *Philos. Trans. R. Soc. London, Ser. B* **1952**, *237*, 37.

[24] C. P. Schenk, M. Or-Guil, M. Bode, H.-G. Purwins, *Phys. Rev. Lett.* **1997**, *78*, 3781.

[25] E. S. Lobanova, F. I. Ataullakhanov, *Phys. Rev. Lett.* **2004**, *93*, 098303.

[26] V. Badescu, P. T. Landsberg, *Semicond. Sci. Technol.* **1993**, *8*, 1267.

[27] D. Redfield, J. P. Wittke, J. I. Pankove, *Phys. Rev. B* **1970**, *2* 1830.

[28] D. R. Cox, *Principles of Statistical Inference*, Cambridge University Press, Cambridge, NY **2006**.

[29] M. Wahl, S. Orthaus-Müller, *Time tagged time-resolved fluorescence data collection in life sciences*, Technical report, PicoQuant GmbH, Berlin **2014**.

[30] W. K. Metzger, I. L. Repins, M. A. Contreras, *Appl. Phys. Lett.* **2008**, *93*, 022110.

[31] M. Maiberg, C. Spindler, E. Jarzembowski, R. Scheer, *Thin Solid Films* **2015**, *582*, 379.

[32] U. Würfel, A. Cuevas, P. Würfel, *IEEE J. Photovolt.* **2015**, *5*, 461.

[33] S. Sze, J. Irvin, *Solid-State Electron.* **1968**, *11*, 599.

[34] M. I. Nathan, W. P. Dumke, K. Wrenner, S. Tiwari, S. L. Wright, K. A. Jenkins, *Appl. Phys. Lett.* **1988**, *52*, 654.

[35] D. M. Tex, T. Ihara, H. Akiyama, M. Imaizumi, Y. Kanemitsu, *Appl. Phys. Lett.* **2015**, *106*, 013905.

[36] M. Großmann, S. Heyder, Repository - Generalized modelling of photoluminescence transients, http://doi.org/10.5281/zenodo.71785760.

[37] C. Rackauckas, Q. Nie, *J. Open Res. Softw.* **2017**, *5*, 17.

[38] Y. Wang, H.-X. Li, T. Huang, L. Li, *Appl. Soft Comput.* **2014**, *18* 232.

[39] R. Feldt, Blackboxoptim.jl, https://github.com/robertfeldt/BlackBoxOptim.jl (accessed: September 2021).

[40] J. Nocedal, *Math. Comput.* **1980**, *35*, 773.

[41] P. McCullagh, J. A. Nelder, *Generalized Linear Models*, Number 37 in Monographs on Statistics and Applied Probability, 2nd ed., Chapman & Hall/CRC, London UK **1998**.

[42] D. E. Aspnes, S. M. Kelso, R. A. Logan, R. Bhat, *J. Appl. Phys.* **1986**, *60*, 754.

[43] E. Centurioni, *Appl. Opt.* **2005**, *44*, 7532.

[44] J. H. Stathis, M. A. Kastner, *Phys. Rev. B* **1987**, *35*, 2972.

[45] R. A. Mair, J. Y. Lin, H. X. Jiang, E. D. Jones, A. A. Allerman, S. R. Kurtz, *Appl. Phys. Lett.* **2000**, *76*, 188.

[46] A. Mitonneau, A. Mircea, G. Martin, D. Pons, *Rev. Phys. Appl.* **1979**, *14*, 853.

[47] L. Samuelson, P. Titze, H. Grimmeiss, *J. Cryst. Growth* **1981**, *55*, 164.

[48] J. S. Blakemore, *J. Appl. Phys.* **1982**, *53*, R123.

[49] H. Amann, *Ordinary Differential Equations: An Introduction to Nonlinear Analysis*, De Gruyter Studies in Mathematics, Vol. *13*, De Gruyter, Berlin, NY **1990**.